Vortex Filtering for Turbulence Models applied to Crossflow Separation

Scott M. Murman
ELORET
Moffett Field, CA 94035
smurman@nas.nasa.gov

Abstract

The application of turbulence models to the flow about slender bodies at high angles of attack poses many difficulties. Regions of three-dimensional crossflow separation and strong vortices outside the boundary layer usually force the modification of standard models which have been developed for attached boundary layers and wake flows. This work examines the performance of three turbulence models for predicting crossflow separation; the Baldwin-Lomax model with corrections due to Degani-Schiff, the Spalart-Allmaras model, and Menter's shear-stress transport (SST) model. These models are applied to the crossflow separation from a smooth tangent-ogive cylinder at $20°$ angle of attack. The current work utilizes a scheme for generating grid-independent solutions for these types of flows. From this it's found that the production of turbulent eddy-viscosity in the leeward vortices must be reduced for the one- and two-equation models to provide accurate results. A vortex filter which is Galilean-invariant and computationally efficient is developed for this purpose. Computed results indicate that this filter can substantially improve the prediction of the surface pressure and crossflow separation locations for the one and two-equation turbulence models considered.

1   Introduction

The simulation of turbulent crossflow separation about slender bodies at high angles of attack poses many difficulties for Computational Fluid Dynamics (CFD) methods. For high Reynolds number flows,[*] the primary difficulty in utilizing Reynolds-averaged Navier-Stokes (RANS) methods is the application of a suitable turbulence model. Many have attempted to extend existing models which perform well for other types of flows, rather than develop a turbulence model specifically for crossflow separation, with varying degrees of success. Most turbulence models are developed and validated by comparison with planar two-dimensional and axisymmetric flows. The extension of these models to highly three-dimensional flows with significant adverse pressure gradients, separated shear layers, and strong vortices outside the boundary layer is challenging.

Many researchers have proposed "fixes" for the Baldwin-Lomax algebraic turbulence model [1] in order determine the correct boundary-layer length scale in the presence of separated free shear layers [2–4]. The correct length scale is critical near the primary crossflow separation location, where an erroneous value can lead to high values of eddy viscosity which delay the crossflow separation (cf. [2, 5] for a detailed discussion). Gee et al. [6] compared several implementations of the Baldwin-Lomax model for computing the flow about a 6:1 prolate spheroid at high angle of attack, and also proposed an extension similar to the Degani-Schiff corrections [2] for the Johnson-King model. Murman and Chaderjian [5] compared two implementations of the Degani-Schiff corrections to the Baldwin-Lomax model for computing the flow about a tangent-ogive cylinder at $\alpha = 20°$, and found that the original implementation is necessary in order to predict the correct primary crossflow separation from smooth bodies.

Gordnier [7] and Murman and Chaderjian [5] examined the application of turbulence models to crossflow separation around a 65°-sweep delta wing with a sharp leading edge. As opposed to the crossflow separation around a smooth slender body, such as a prolate spheroid or ogive cylinder, the primary crossflow separation location around a delta wing is fixed at the sharp leading edge. As such, the behavior of the turbulence model near the primary crossflow sepa-

[*]This work focuses solely on fully-developed turbulent flows. It's acknowledged that transitional effects can have a significant role in flows with crossflow separation, however the coupled effects of transition and turbulent separation are beyond the scope of the current work.

ration location becomes relatively unimportant for these types of configurations. Gordnier examined methods of reducing the production of eddy viscosity in the strong leeward vortices for the Jones and Launder $k - \epsilon$ model. Murman and Chaderjian examined similar fixes for the Spalart-Allmaras one-equation model. Neither of these efforts could provide results of the same accuracy as achieved using the Degani-Schiff corrections to the Baldwin-Lomax model.

This study is an extension of the work of [5]. One of the results in that previous study states "(the large values of eddy-viscosity in the leeward vortices) does not appear to adversely affect the prediction of the aerodynamic loading ...", when speaking of the Spalart-Allmaras model. It will be shown that this statement is only true when a relatively coarse grid resolution is utilized. Continued grid refinement can actually degrade the performance of the one- and two-equation models that have been studied for these types of flows. When "grid-independent" solutions are obtained, then the opposite statement is true; in order to achieve good agreement with experimental results it's necessary to reduce, or even eliminate, the turbulent eddy-viscosity in the leeward-side vortices. The current work first identifies grid-independent computed results for these types of complex flows. Once this is achieved, then the behavior of the turbulence models can be reliably evaluated, and proposed modifications tested.

The current work examines three turbulence models applied to crossflow separation at high angles of attack; the algebraic Baldwin-Lomax model with corrections due to Degani-Schiff (B-L/D-S), the one-equation Spalart-Allmaras model (S-A) [8], and Menter's two-equation shear-stress transport (SST) model [9]. Methods for reducing (or eliminating) the production of turbulent eddy-viscosity in the leeward vortices are analyzed for both the S-A and SST models. A Galilean-invariant leeward vortex filter has been developed and preliminary results indicate that it can greatly improve the performance of linear transport closure models for flows with crossflow separation. The base models and the modifications will be evaluated the tangent-ogive cylinder experimental data of Lamont at $\alpha = 20°$ [10]. This experimental data set was chosen because it contains fully-developed turbulent crossflow separation. The major emphasis of this work is prediction of the aerodynamic force due to pressure. This is seen as a necessary first step before proceeding to skin-friction distributions.

The first section of this work briefly describes the numerical scheme that was utilized, and then a method for obtaining grid-independent simulations for these types of separated flows is detailed. The computed results for the tangent-ogive cylinder are then reported. The development of a free vortex filter is outlined, and then applied to the tangent-ogive cylinder configuration. Finally, a summary and some directions for future work are presented.

2   Numerical Method

This work deals with numerical modeling of three-dimensional separated flowfields. In order to accurately simulate the physics of these flows, it is necessary to use the Navier-Stokes equations as a physical model. The complete Navier-Stokes equations are often simplified using the "thin-layer" approximation [11] when performing high Reynolds number flow simulations, and this has been maintained in the current work to reduce the computational costs.

The diagonalized version of the Beam and Warming factored scheme due to Pulliam and Chausee [12] is used throughout. The OVER-FLOW finite-difference solver (version 1.8f) [13] is used for all of the computed solutions, and the implementations of the various turbulence models, with the exception of the Degani-Schiff corrections which are implemented as described in [2]. The mean flowfields examined in this work are known to be "steady" from the experimental investigations, and convergence acceleration techniques (local time-stepping, multi-grid) were utilized. All computed simulations were converged until a steady-state was observed.

3   Grid Independence

This section describes the strategy that was used to develop grid-independent solutions. The distribution of grid points is considered fixed in the axial and circumferential directions in order to reduce the number of independent parameters. The axial and circumferential distributions were chosen based on experience from previous computed results, as were the dimensions of the computational domain. To date, this has not been found to be a serious limitation to predicting the pressure field, however if necessary circumferential refinement (for example) could simply be performed as an additional step.

A schematic of a crossflow grid plane is shown in Fig. 1. The grid clustering in the body-normal direction is broken into three regions; the near-wall region, the region through the boundary layer and outer vortices, and the far-field region. The properties of the grid resolution in each region are described in Fig. 1 and Table 1, where R and D are the radius and diameter of the body, respectively, $\tilde{r} \equiv \frac{r-R}{D}$ is the radial distance, N is the number of points within each region, and SR is the cell stretching ratio, or growth factor. The near-wall region contains uniform spacing, and is characterized by the height of the first cell above the body surface ($\Delta \tilde{r}_0$). The vortex and far-field

Region	Variable	Induced	Fixed
Near-Wall	$\Delta\tilde{r}_0$	$\tilde{r}_{max}$	$SR_{max}(=1.0)$, $N(=5)$
vortex	N	$\Delta\tilde{r}_0$ (from Region 1)	$SR_{max}(=1.2)$, $\tilde{r}_{max}(=3.0)$
Far-field	N	$\Delta\tilde{r}_0$ (from Region 2)	$SR_{max}(=1.2)$, $\tilde{r}_{max}(=12.0)$

Table 1: Body-normal grid spacing parameters.

regions are both stretched in the body-normal direction (cell volumes increase with distance from the body surface), and are characterized by the number of points within each region.
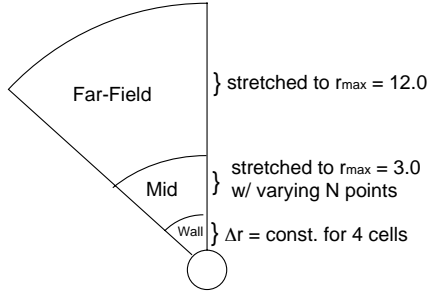

Figure 1: Regions of body-normal grid spacing.

Figure 2: Tangent-ogive surface pressure distribution (S-A model, $x/D = 5.0$, $M_\infty = 0.2$, $\alpha = 20°$, $Re_D =4.0$ x 10^6) ——— $\Delta\tilde{r}_0 =1.0$ x 10^{-4}, - - - - - $\Delta\tilde{r}_0 =1.0$ x 10^{-5}, — · — $\Delta\tilde{r}_0 =1.0$ x 10^{-6}, •, ○ Exp. Left, Right [10].

The resolution of the windward boundary layer and the leeward vortices are treated separately. Initially, refinement is performed solely in the near-wall region in order to accurately resolve the attached boundary layer. The outer regions are created utilizing the maximum prescribed stretching ratio. The surface pressure distribution for the tangent-ogive cylinder configuration at $x/D = 5.0$, computed using the Spalart-Allmaras model, is shown in Fig. 2 as an example.* The average and maximum computed values of y^+ for the complete computational domain are found in Table 2. It's seen that changes occur in the attached boundary layer around $\phi = 90°$ after the mesh with the coarsest near-wall spacing is refined, however either of the finer grids is suitable. Based on these calculations, a near-wall spacing of $\Delta\tilde{r}_0 =1.0$ x 10^{-5} was utilized, and a resolution study of the vortex region was performed with this fixed value.

The refinement of the boundary-layer/vortex region was performed by increasing the number of points within this region, for fixed near-wall and far-field regions, where the choice of the near-wall spacing was described above. Fig. 3 shows a typical example of this process for the tangent-ogive configuration and the B-L/D-S and S-A models, where the number of points in the vortex region are listed. The corresponding computed normal force coefficients for these computations are found in Table. 3. Note that the force due

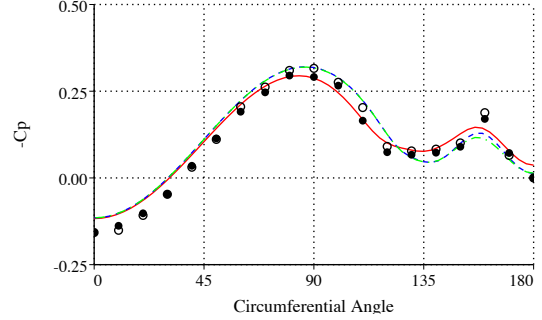*A detailed discussion of the geometry and experimental data will be presented in Sec. 4.

to pressure accounts for approximately 99% of the computed normal force for this configuration. It's seen that the comparison between the computed pressure peak due to the primary vortex (near $\phi = 160°$) and the experimental data actually degrades as the vortex region is refined in the simulation using the Spalart-Allmaras model, while with the B-L/D-S model the grid refinement leads to an improvement in the predicted leeward-side pressure distribution. This grid sensitivity is not limited to the Spalart-Allmaras model or the tangent-ogive cylinder configuration, and care must be taken when comparing computed results as simulations on a coarse mesh may fortuitously appear positive. The differences in the computed pressure for the computations utilizing 78 and 88 points within the vortex region are minor, and hence a final grid configuration with a near-wall spacing of $\Delta\tilde{r}_0 =1.0$ x 10^{-5} and 78 points in the vortex region (91 overall in the body-normal direction) would be utilized for all subsequent computations.

4 Tangent-Ogive Cylinder Computations

The tangent-ogive cylinder geometry used in this study consists of a 3.5 diameter tangent-ogive forebody section, with a 7.0 diameter cylindrical portion extending aft of the ogive section.

3

Model	$\Delta\tilde{r}_0 =1.0 \times 10^{-4}$	$\Delta\tilde{r}_0 =1.0 \times 10^{-5}$	$\Delta\tilde{r}_0 =1.0 \times 10^{-6}$
B-L/D-S	8.55/12.50	1.64/2.73	0.17/0.30
S-A	8.58/13.62	1.64/2.53	0.17/0.28

Table 2: Average/maximum y^+ values for tangent-ogive near-wall refinement ($M_\infty = 0.2$, $\alpha = 20°$, $Re_D =4.0 \times 10^6$).
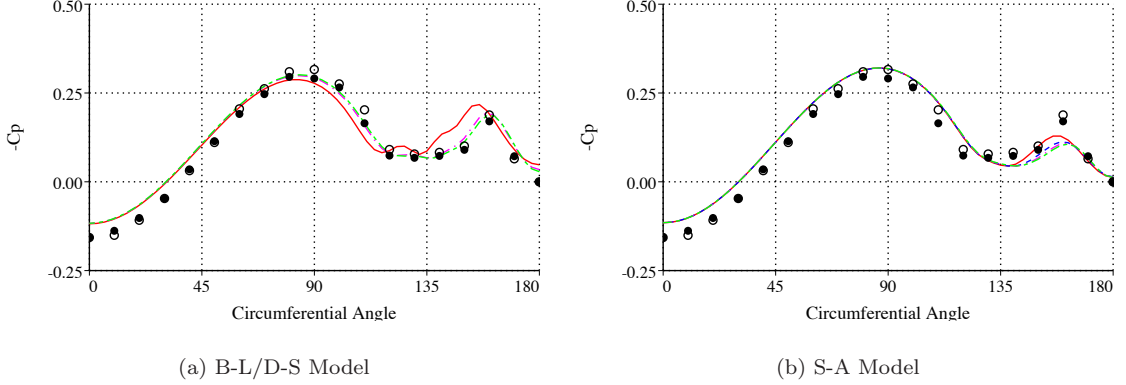

(a) B-L/D-S Model

(b) S-A Model

Figure 3: Tangent-ogive surface pressure distribution ($x/D = 5.0$, $M_\infty = 0.2$, $\alpha = 20°$, $Re_D =4.0 \times 10^6$) —— $N_{pt} = 58$, – – – – $N_{pt} = 68$, $\cdots\cdots$ $N_{pt} = 78$, $\cdot$ – – – $\cdot$ $N_{pt} = 88$ •, ○ Exp. Left, Right [10].

Model	$N_{pt} = 58$	$N_{pt} = 68$	$N_{pt} = 78$	$N_{pt} = 88$
B-L/D-S	1.47	N/A	1.36	1.35
S-A	1.15	1.12	1.12	1.12

Table 3: Computed normal force coefficient ($M_\infty = 0.2$, $\alpha = 20°$, $Re_D = 4.0 \times 10^6$).

This geometry was tested in the NASA Ames 12-ft wind tunnel by Lamont [10]. The computed flow conditions are $M_\infty = 0.2$, $\alpha = 20°$, and $Re_D = 4.0 \times 10^6$. The computational grid that resulted from the grid-independence procedure described in Sec. 3 contains 67 points in the axial direction, 61 points in the circumferential direction (half-body configuration with uniform circumferential spacing of $\Delta\phi = 3.0°$), and 91 points in the body-normal direction. A visualization of a typical computed flowfield is shown in Fig. 4 for reference. The crossflow separation and roll-up of the shear layer into a strong primary vortex on the leeward-side of the body is clearly evident.

Experimental pressures are provided for both the left and right sides of the lateral symmetry plane to emphasize that the flow remains symmetric for this configuration, and hence a half-body simulation is appropriate. The experimental surface pressure near the windward symmetry plane is consistently higher than the computed results for all of the simulations performed in this
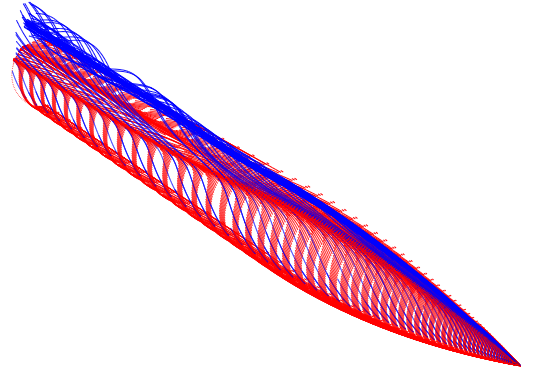

Figure 4: Tangent-ogive cylinder computed flow structures

study. This is not unique to the current work, and similar trends are seen in previous studies [3–5, 14]. Degani et al. [14] note that "... this is the result of the high-angle-of-attack flow condition, in which the windward flow was directed

4

into the pressure taps." Thus, the measured pressure near the windward symmetry plane would be greater than the static pressure, however the measured static pressure on the remainder of the body, exclusive of the flow reattachment near the leeward symmetry plane, should be accurate. A cross-sectional plane located at $x/D = 5.0$ has been used for all of the comparisons with the experimental data in this work. This plane was chosen because it is located far downstream from the experimental laminar and transitional regions near the tip of the model, and yet is still far enough upstream from the aft end of the model to eliminate any mounting or aft-body effects.[*]

Figure 5 shows the surface pressure distribution and wall shear stress distribution ($\frac{\tau_w}{\rho U_\infty^2}$) for the simulations using the three base turbulence models. The wall shear stress is broken into streamwise and crossflow components. It's seen that the B-L/D-S simulation is in relatively good agreement with the experimental pressure data, while the S-A and SST models do not agree as well, especially in the prediction of the suction peak near $\phi = 160°$ due to the primary vortex. The crossflow wall shear stress distribution shows that the B-L/D-S model is predicting a crossflow separation location furthest upstream. The is likely due to the stronger primary vortex in this simulation. The stronger primary vortex induces a stronger secondary flow, which forces the crossflow separation location upstream. It's seen that the correlation between the primary crossflow separation and the strength of the primary vortex suction peak is consistent for all three models.

5   Vortex Filtering

In order to understand the discrepancy between the computed and experimental pressures seen in Fig. 5, the behavior of the Spalart-Allmaras was investigated further. The S-A model was chosen rather than the SST model as it's a simpler one-equation model. The S-A model produces large, spurious values of eddy-viscosity in the region of the leeward vortices for flows with crossflow separation (cf. Fig. 9 in [5]). The SST model has a similar deficiency (cf. [7]). The cause of these large values in the S-A model is the eddy-viscosity production term of the model

$$P = c_{b1}\nu_t|\omega| \tag{1}$$

where c_{b1} is a scalar coefficient, ν_t is the turbulent eddy-viscosity, and ω is the vorticity. In the leeward vortices ω is large and the production of turbulent eddy-viscosity increases. As a result, the eddy-viscosity in the primary vortex region can be orders-of-magnitude larger than even

the value in the attached boundary layer.[†] This large viscosity diffuses and weakens the primary leeward vortex, and by induction the secondary vortex as well. In order to determine if this effect caused the discrepancy seen in Sec. 4, two numerical experiments were performed. First, the magnitude of the crossflow vorticity (i.e. the vorticity component in the crossflow direction, ω_ϕ) was utilized in the production term of the S-A model. Since the flow direction of the attached boundary layers is still mainly in the streamwise direction, only utilizing the crossflow vorticity should reduce the production slightly within the attached boundary layers, and remove it almost altogether outside the boundary layer. This change did greatly improve the correlation between the computed and measured surface pressures using the S-A model. In order to determine whether the reduction of eddy-viscosity production within the boundary layer or in the outer flow caused the improvement, a second experiment was performed where the production was proportional to the crossflow vorticity magnitude within the boundary layer, and to the total vorticity magnitude outside the boundary layer. In this case no substantial improvement was seen over the results of the baseline S-A model shown in Fig. 5. Hence it's felt that reducing (or eliminating) the eddy-viscosity in the leeward-region vortices is required.

Several modifications have been proposed for reducing the production of turbulent eddy-viscosity in strong vortices outside the boundary layer for the S-A and other one- and two-equation models. Spalart and Shur developed a correction which accounts for streamline curvature effects [15], and which has been tested for wingtip trailing vortices [16], however the correction requires derivatives of the strain-rate tensor which makes it computationally prohibitive. Burr et al. [17] recommend a simpler curvature correction term, similar to a turbulent Richardson number, which is proportional to $\frac{\partial U_i}{\partial x_j}\frac{\partial U_j}{\partial x_i}$. Menter [9] recommends limiting the production of turbulent kinetic energy in the $k - \epsilon$ and $k - \omega$ models. Finally, Dacles-Mariani et al. [18] were able to reduce the dissipation of wingtip vortices by essentially making the production of eddy-viscosity proportional to the magnitude of the strain-rate tensor, S_{ij}, rather than the vorticity. The computed variation of vorticity magnitude, crossflow vorticity magnitude, and strain-rate magnitude for the simulation of the tangent-ogive cylinder using the S-A model, at a circumferential location

---

[†]While turbulent stresses are present in the free shear layers and viscous core region of a vortex, these values are relatively small and localized, as opposed to the extremely large eddy-viscosity values found through the entire leeward-vortex region in the simulations. This indicates that the turbulent eddy-viscosity production in these regions is a numerical artifact, not the result of a consistent physical model.
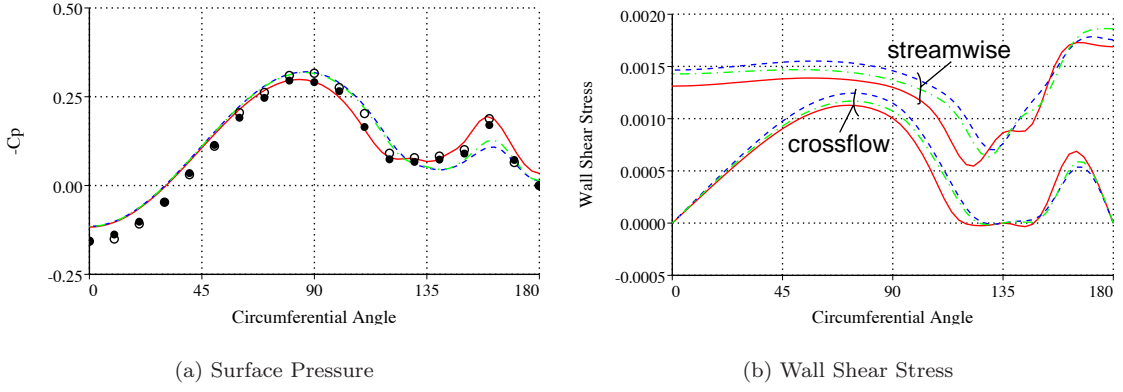
(a) Surface Pressure

(b) Wall Shear Stress

Figure 5: Tangent-ogive cylinder surface distributions ($x/D = 5.0$, $M_\infty = 0.2$, $\alpha = 20°$, $Re_D = 4.0$ x 10^6) ———— B-L/D-S model, - - - - S-A model, — · — SST model, ●, ○ Exp. Left, Right [10].

of $\phi = 159°$ (passing through the primary vortex), is shown in Fig. 6. The edge of the boundary layer is located at approximately $\tilde{r} = 1.0$ x 10^{-3} for this computation, and the primary vortex lies between $0.05 \leq \tilde{r} \leq 0.3$. It's seen that the cross-flow vorticity is about one order of magnitude lower than the vorticity magnitude through the vortex region, while there is little practical difference between the strain-rate and vorticity in this region. In other parts of the flow, the strain-rate magnitude can actually exceed the vorticity magnitude outside the boundary layer. Tests using a magnitude of strain-rate eddy-viscosity production term did not show an improvement in the behavior of the S-A model. From these considerations, the strain-rate tensor does not appear to be a useful eddy-viscosity production limiter for these types of flows.
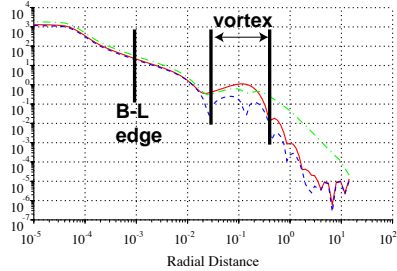

Figure 6: Tangent-ogive velocity gradient tensor scalar norms ($x/D = 5.0$, $\phi = 159°$, $M_\infty = 0.2$, $\alpha = 20°$, $Re_D = 4.0$ x 10^6) ———— $|\omega|$ — — — $|\omega_\phi|$, — · — $|S_{ij}|$

The effectiveness of any turbulence model modification for these types of flows is related to the ability to distinguish between the vorticity within the boundary layer, and the free vortices outside the boundary layer. Once the distinction between the boundary layer and leeward vortices can be made, then the vortex region can be "filtered" from the turbulence model. The Degani-Schiff correction to the Baldwin-Lomax model is effective because it achieves just this aim. The curvature term of Burr et al. is able to discriminate between the two sources of vorticity, as it changes sign when the primary vortex is encountered, however this term has difficulty when encountering secondary vortices and in other regions outside the boundary layer. One advantage that the curvature correction terms of both Burr et al. and Spalart and Shur possess is that they are Galilean-invariant. Since most turbulence models are developed to be Galilean-invariant, it's desirable that any model correction term maintain this feature. Examining the velocity-gradient tensor, the three invariants that result directly from computing the principal directions are

$$I_1 = \text{trace}\left(\frac{\partial U_i}{\partial x_j}\right) = U_x + V_y + W_z$$

$$I_2 = \begin{vmatrix} U_x & V_x \\ U_y & V_y \end{vmatrix} + \begin{vmatrix} V_y & W_y \\ V_z & W_z \end{vmatrix} + \begin{vmatrix} U_x & W_x \\ U_z & W_z \end{vmatrix}$$

$$I_3 = \left|\frac{\partial U_i}{\partial x_j}\right|$$

Other invariants can be formed from combinations of these three (e.g. $\frac{\partial U_i}{\partial x_j}\frac{\partial U_i}{\partial x_j} = I_1^2 - 2I_2$). Of these three invariants, only I_2 reliably responds to vorticity outside the boundary layer, however it cannot distinguish between a free vortex and vorticity within the boundary layer. This can be

6

remedied by scaling I_2 by the local cell volume, $\mathcal{V}$ (small cells within the boundary layer receive much less of a contribution than larger ones in the vortex region), which is also invariant. Borrowing the notation from signal processing, we then have that the vortex filter H'_v is

$$H'_v \propto I_2 \mathcal{V}$$

In order to determine whether the behavior of H'_v is simply the result of a particular grid resolution, or is independent of the mesh, $I_2\mathcal{V}$ was calculated from each computed simulation (5 different grid-point densities) at $x/D = 5.0$, $\phi = 159°$. As can be seen from Fig. 7, the quantity $I_2\mathcal{V}$ converges as the mesh is refined, and does easily distinguish the primary vortex.
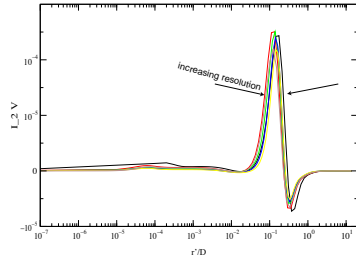

Figure 7: Vortex filter term for all computed tangent-ogive cylinder simulations ($x/D = 5.0$, $\phi = 159°$, $M_\infty = 0.2$, $\alpha = 20°$, $Re_D =$4.0 x 10^6)

The vortex filter must be modified in order to use it directly in a numerical scheme. The absolute value of H'_v is utilized, and then the hyperbolic tangent is formed in order to achieve a smooth variation, and to limit the maximum value of the function. The final form becomes

$$H_v = \tanh\left(\frac{|I_2\mathcal{V}|}{H_{max}}\right) \qquad (2)$$

H_{max} was determined by numerical experiment, and a value of 5.0 x 10^{-6} has been found to give good results for all of the computed results in this work.

5.1 S-A model

Equation 2 can be applied to the S-A model by modifying the production term (Eqn. 1) as

$$P' = P(1 - H_v) \qquad (3)$$

This reverts to the original formulation within the boundary layer ($H_v \to 0$), and removes the production of eddy-viscosity in the leeward-side vortices ($H_v \to 1$). When the vortex filter is applied to the S-A model,* the computed results

*The filtered S-A model is referred to as the H_v S-A model in the figures.

are in much better agreement with the experimental measurements (cf. Fig. 8). It's also seen that both the strength of the primary vortex and the primary crossflow separation location are now in good agreement between the B-L/D-S model and the filtered S-A model. The computed normal force for the filtered S-A model is $C_N = 1.29$ (c.f. Table 3). Further, as the grid refinement is increased the filtered S-A model computations now progressively improve (Fig. 9), similar to the behavior of the B-L/D-S model, as opposed to the degradation seen in the baseline S-A model (cf. Fig. 3).
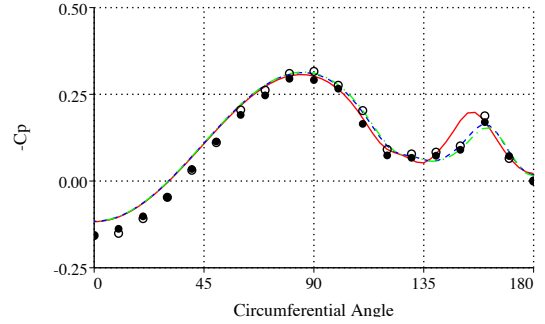

Figure 9: Tangent-ogive surface pressure distribution (H_v S-A model, $x/D = 5.0$, $M_\infty = 0.2$, $\alpha = 20°$, $Re_D =$4.0 x 10^6) ———— $N_{pt} = 58$, - - - - - $N_{pt} = 78$, · — — — · $N_{pt} = 88$ •, ∘ Exp. Left, Right [10].

5.2 SST model

The free vortex filter can also be utilized to improve the prediction of the surface pressure using Menter's two-equation SST model. In general terms, the two-equation models take the form

$$\frac{D(k,\omega)}{Dt} = Production - Dissipation - Diffusion$$

Space precludes including the details of each term, which can be found in [9]. There are many ways in which the vortex filter can be applied to a complicated two-equation model. One approach which has proven successful is to filter both the production and dissipation terms, while leaving the diffusion terms untouched. The rationale is that the production and dissipation are directly proportional to mean flow quantities (which will be dependent upon the separated flow structures), while the diffusion terms are dependent upon gradients of turbulence quantities which should not require modification if the model itself remains well-behaved. The filtered
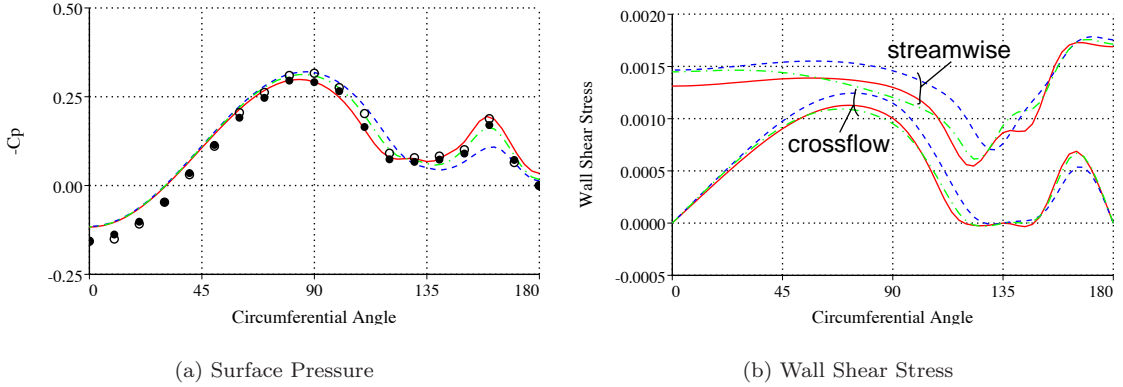
7

(a) Surface Pressure

(b) Wall Shear Stress

Figure 8: Tangent-ogive cylinder surface distributions ($x/D = 5.0$, $M_\infty = 0.2$, $\alpha = 20°$, $Re_D =$ 4.0 x 10^6) ———— B-L/D-S model, - - - - S-A model, — · — H_v S-A model, ●, ○ Exp. Left, Right [10].

SST model (H_v SST) then becomes

$$\frac{D(k, \omega)}{Dt} = (Production - Dissipation)(1 - H_v)$$
$$- Diffusion$$

(4)

This again reverts to the original formulation within the boundary layer.

The computed distributions of the surface pressure and shear stress for all of the filtered models are shown in Fig. 10. The filtered S-A and SST models predict very similar pressure distributions, and all three models show good agreement with the experimental data. The computed normal force for the filtered SST model is $C_N = 1.33$. The filtered SST model shows a large decrease in wall shear stress in the attached flow region, however all three models predict the same primary crossflow separation location. Without detailed experimental shear stress data, it's difficult to make any statements about the accuracy of the models in predicting wall stress.

5.3 Baldwin-Lomax model

The vortex filter can also be used to improve the performance of the standard Baldwin-Lomax model. As has been seen, the Degani-Schiff modifications can be utilized, however these modifications are dependent upon the topology of the computational mesh, and hence are difficult to implement in general production flow solvers and for complicated geometries. The main difficulty in applying the Baldwin-Lomax model to flows with crossflow separation concerns determining the proper length scale for the model in the presence of vortices outside the boundary layer. This is caused by the behavior of the function $F(y)$, which is a function of the local vorticity (cf. Fig. 3

of [5]). This can be easily remedied by modifying the length scale function as

$$F'(y) = F(y)(1 - H_v)$$

(5)

In this manner the peak of $F'(y)$ within the boundary layer is unambiguous, and the standard Baldwin-Lomax model can be applied directly. No computed results using this filtered Baldwin-Lomax model are available for the tangent-ogive cylinder configuration considered in this work, however preliminary results with other configurations indicates the filtered model does provide results on par with the Degani-Schiff modifications.

6 Summary

A free vortex filter for flows with crossflow separation has been developed which is Galilean-invariant, and computationally inexpensive. By applying the filter appropriately for each of the Baldwin-Lomax, Spalart-Allmaras, and SST models, it was possible to greatly improve the prediction of the pressure distribution on the body for a tangent-ogive cylinder at high angle of attack. This work was a preliminary "proof-of-concept" study, and it's expected that this type of filter will continue to evolve as more experience is gained with different turbulence models and configurations. It's desirable to extend the current work by simulating a delta wing configuration at high angle at attack, and to test the technique with flows at transonic and supersonic Mach numbers. From the experience gained with these diverse simulations it's hoped that the empirical constant H_{max}, which is likely configuration dependent, can be replaced. These subjects remain for future work.
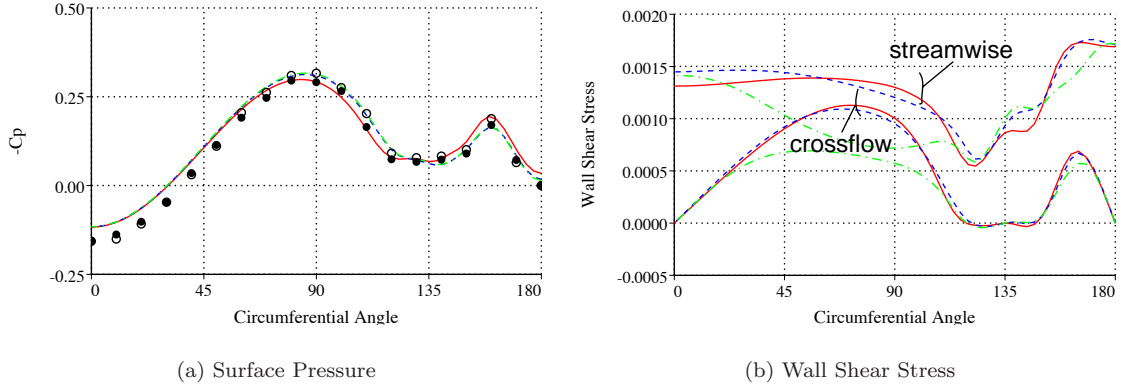
(a) Surface Pressure   (b) Wall Shear Stress

Figure 10: Tangent-ogive cylinder surface distributions ($x/D = 5.0$, $M_\infty = 0.2$, $\alpha = 20°$, $Re_D =4.0$ x 10^6) ——— B-L/D-S model, - - - - - H_v S-A model, — · — H_v SST model, •, ∘ Exp. Left, Right [10].

References

[1] Baldwin, B.S., and Lomax, H., "Thin Layer Approximation and Algebraic Model for Separated Turbulent Flows," AIAA Paper 78-0257, Jan. 1978.

[2] Degani, D., and Schiff, L. B., "Computation of Turbulent Supersonic Flows About Pointed Bodies Having Crossflow Separation," *Journal of Computational Physics*, vol. 66, pp. 183–196, Sept. 1986.

[3] Hartwich, P.M. and Hall, R.M., "Navier-Stokes Solutions for Vortical Flows Over a Tangent-Ogive Cylinder," *AIAA Journal*, vol. 28, no. 7, pp. 1171–1179, 1990.

[4] Vatsa, V.N., "Viscous Flow Solutions for Slender Bodies of Revolution at Incidence," *Computers and Fluids*, vol. 20, no. 3, pp. 313–320, 1991.

[5] Murman, S.M. and Chaderjian, N.M., "Application of Turbulence Models to Separated High-Angle-of-Attack Flows," AIAA Paper 98-4519, Aug. 1998.

[6] Gee, K., Cummings, R. M., and Schiff, L. B., "Turbulence Model Effects on Separated Flow About a Prolate Spheroid," *AIAA Journal*, vol. 30, pp. 655–664, Mar. 1992.

[7] Gordnier, R.E., "Computational Study of a Turbulent Delta-Wing Flowfield using Two-Equation Turbulence Models," AIAA Paper 96-2076, June 1996.

[8] Spalart, P. R., and Allmaras, S. R., "A One-Equation Turbulence Model for Aerodynamic Flows," AIAA Paper 92-0439, Jan. 1992.

[9] Menter, F.R., "Zonal Two Equation $k - \omega$ Turbulence Models for Aerodynamic Flows," AIAA Paper 93-2906, July 1993.

[10] Lamont, P.J., "Pressures Around an Inclined Ogive Cylinder with Laminar, Transitional, or Turbulent Separation," *AIAA Journal*, vol. 20, pp. 1492–1499, Nov. 1982.

[11] Steger, J.L., "Implicit Finite-Difference Simulation of Flow About Arbitrary Two-Dimensional Geometries," *AIAA Journal*, vol. 16, pp. 679–686, July 1978.

[12] Pulliam, T.H. and Chausee, D.S., "A Diagonal Form of an Implicit Approximate-Factorization Algorithm," *Journal of Computational Physics*, vol. 39, pp. 347–363, Feb. 1981.

[13] Buning, P.G., Jesperson, D.C., Pulliam, T.H., Chan, W.M., Slotnick, J.P., Krist, S. E., and Renze, K.J., *OVERFLOW User's Manual*. NASA.

[14] Degani, D., Schiff, L. B., and Levy, Y., "Numerical Prediction of Subsonic Turbulent Flows over Slender Bodies at High Incidence," *AIAA Journal*, vol. 29, pp. 2054–2061, Dec. 1991.

[15] Spalart, P. R., and Shur, M., "On the Sensitization of Turbulence Models to Rotation and Curvature," *Aerospace Science and Technology*, no. 5, 1997.

[16] Shur, M., Strelets, M., Travin, A., Spalart, P.R., "Two Numerical Studies of Trailing Vortices," AIAA Paper 98-0595, Jan. 1998.

[17] Burr, R.C., Menter, F.R., Grotjans, H., and Frühauf, H.H., "Development of a Curvature Correction Method for the $k - \epsilon$ Turbulence Model," in *ECCOMAS* (Papailon et al., ed.), pp. 1105–1110, John Wiley & Sons, 1998.

[18] Dacles-Mariani, J., Zilliac, G.G., Chow, J.S., Bradshaw, P., "Numerical/Experimental Study of a Wingtip Vortex in the Near Field," *AIAA Journal*, vol. 33, pp. 1561–1568, Sept. 1995.